

Eddy-induced transport of the Kuroshio warm water around the Ryukyu Islands in the East China Sea

Yuki Kamidaira¹, Yusuke Uchiyama² and Satoshi Mitarai³

1. Corresponding author: Nuclear Science and Engineering Center, Japan Atomic Energy Agency, Tokai, Ibaraki, Japan (email: kamidaira.yuki@jaea.go.jp)
2. Department of Civil Engineering, Kobe University, Kobe, Hyogo, Japan (email: uchiyama@harbor.kobe-u.ac.jp)
3. Marine Biology Unit, Okinawa Institute of Science and Technology, Onna, Okinawa, Japan (email: satoshi@oist.ac.jp)

Abstract

In this study, an oceanic downscaling model in a double-nested configuration was used to investigate the role played by the Kuroshio warm current in preserving and maintaining biological diversity in the coral coasts around the Ryukyu Islands (Japan). A comparison of the modeled data demonstrated that the innermost submesoscale eddy-resolving model successfully reproduced the synoptic and mesoscale oceanic structures even without data assimilation. The Kuroshio flows on the shelf break of the East China Sea approximately 150–200 km from the islands; therefore, eddy-induced transient processes are essential to the lateral transport of material within the strip between the Kuroshio and the islands. The model indicated an evident predominance of submesoscale anticyclonic eddies over cyclonic eddies near the surface of this strip. An energy conversion analysis relevant to the eddy-generation mechanisms revealed that a combination of both the shear instability due to the Kuroshio and the topography and baroclinic instability around the Kuroshio front jointly provoke these near-surface anticyclonic eddies, as well as the subsurface cyclonic eddies that are shed around

35 the shelf break. Both surface and subsurface eddies fit within the submesoscale, and
36 they are energized more as the grid resolution of the model is increased. An eddy
37 heat flux (EHF) analysis was performed with decomposition into the divergent
38 (dEHF) and rotational (rEHF) components. The rEHF vectors appeared along the
39 temperature variance contours by following the Kuroshio, whereas the dEHF
40 properly measured the transverse transport normal to the Kuroshio's path. The
41 diagnostic EHF analysis demonstrated that an asymmetric dEHF occurs within the
42 surface mixed layer, which promotes eastward transport toward the islands.
43 Conversely, below the mixed layer, a negative dEHF tongue is formed that promotes
44 the subsurface westward warm water transport.

45

46 *Key words:* submesoscale eddy, Kuroshio, topography, East China Sea, ROMS

47

48 **1. Introduction**

49

50 Coral reefs are home to the most diverse range of marine life in the world. They
51 are of great importance to marine ecosystems, hosting favorable habitat to a wide
52 variety of flora and fauna. An estimated 25% of all marine life is supported by coral
53 reefs, even though they cover <0.1% of the world's oceans and represent one of the
54 most fragile and endangered marine ecosystems in the world (*e.g.*, Spalding *et al.*,
55 2001). Coral reefs also represent a vital resource for humankind in terms of
56 tourism and fishing. Cesar *et al.* (2003) reported that coral reefs provide
57 approximately US\$29.8 billion in net benefit streams per annum in goods and
58 services to world economies, including tourism (US\$9.6 billion), fisheries (US\$5.7
59 billion), and coastal protection (US\$9.0 billion). Similarly, coral reefs have great
60 economic value in Japan, generating as much as US\$1.6 billion per annum
61 domestically. In particular, the Ryukyu Islands, located in the subtropical region of
62 Japan that fringes the East China Sea (ECS; **Fig. 1**), have ecologically abundant coral
63 reefs situated at their northernmost end at the border between the Pacific and
64 Indian oceans. These corals lie within a region that supports the highest diversity of
65 indigenous species in the world.

66 Water temperature is widely known as a factor that has considerable effect on
67 coral growth. The ideal range of ambient temperature for reef corals is narrow;
68 most corals cannot survive in temperatures much below 16°C–18°C even for a few
69 weeks. High temperatures also have a serious effect on coral growth and can lead to

70 “coral bleaching,” a process that results in devastating mass mortality of the coral
71 during which they expel their symbiotic algae. Therefore, the habitat of coral is
72 generally restricted to a latitudinal band between 30°N and 30°S because
73 decreasing temperature follows increasing latitude.

74 The sea around the Ryukyu Islands in the ECS, located between 25°N and 30°N,
75 provides an environment for coral growth even though it lies at the northernmost
76 extreme of the habitable region. Major warm currents, such as the Kuroshio, allow
77 the development of reefs up to and beyond the ordinary habitable latitudinal limit.
78 These ocean currents play important roles in transporting coral larvae and warm
79 water to such areas, thus maintaining favorable environments for reef corals.

80 The Kuroshio, which is one of the world’s major western boundary currents of
81 the North Pacific subtropical gyre, enters the ECS from the east coast of Taiwan. It
82 turns northeastward and drifts along the continental shelf slope fringing the ECS
83 around the Ryukyu Islands (Qiu, 2001). The Kuroshio not only plays an essential
84 role in the meridional transport of large amounts of warm and salty tropical water
85 northward (*e.g.*, Ichikawa and Beardsley, 1993; Ichikawa and Chaen^[SEP], 2000;
86 Imawaki *et al.*, 2001; Johns *et al.*, 2001; Andres *et al.*, 2008; Yang^[SEP] *et al.*, 2011) but
87 also influences the regional climatic system of the ECS (*e.g.*, Xu *et al.*, 2011; Sasaki
88 *et al.*, 2012). Temperature measurements recorded continuously by more than 100
89 thermometers in conjunction with satellite SST (sea surface temperature)
90 measurements have revealed that areas of high SST are formed off the middle of the
91 west coast of Okinawa Island because of the Kuroshio warm water (Nadaoka *et al.*,
92 2001).

93 Several numerical studies have been undertaken to investigate the
94 physical processes and effects of the Kuroshio in the ECS. Guo *et al.* (2003) were
95 successfully demonstrated that the path and vertical structure of the Kuroshio in
96 the ECS are reproduced more realistically as the horizontal resolution of a model
97 increases on the basis of a triply nested ocean modeling using the Princeton Ocean
98 Model (Blumberg and Mellor, 1987). Based on a study using the Meteorological
99 Research Institute Community Ocean Model (Usui *et al.*, 2006), Usui *et al.* (2008)
100 reported that frontal waves are generated as a result of the collisions between
101 anticyclonic mesoscale eddies with diameters at orders of 100 km. These eddies are
102 considered to have nontrivial influence on mass and heat transport between the
103 Kuroshio and the Ryukyu Islands. Their study suggested that eddy-induced lateral
104 mixing must be substantial to promote the warm water intrusion toward the

105 Ryukyu Islands, because the main body of the Kuroshio is persistently located
106 approximately 150–200 km to the west of the islands, restricting its direct impact.

107 Recently, the effects of submesoscale eddies (at typical horizontal scales of
108 several to tens of km or less) on the mean oceanic structure, stratification, and
109 frontal processes have been studied actively to enhance our understanding of the
110 dynamic processes of the upper oceans (*e.g.*, Boccaletti *et al.*, 2007; Badin *et al.*,
111 2011; Callies *et al.*, 2015; Kunze *et al.*, 2015). Capet *et al.* (2008) conducted a
112 high-resolution numerical experiment of the idealized California Current System
113 using the Regional Oceanic Modeling System (ROMS; Shchepetkin and McWilliams,
114 2005, 2008). They demonstrated that submesoscale eddies occur through
115 frontogenesis, which sharpens the surface density fronts, forming in the regions of
116 high strain on the flanks of mesoscale eddies, down to horizontal scales of a few
117 kilometers or less in association with strong vertical ageostrophic secondary
118 circulations in the surface boundary layer. A multiple nesting technique (*e.g.*,
119 Marchesiello *et al.*, 2003; Penven *et al.*, 2006; Mason *et al.*, 2010) has enabled
120 submesoscale eddy-resolving ocean modeling to investigate submesoscale stirring
121 and mixing in the upper oceans and associated material dispersal. For example,
122 Romero *et al.* (2013) conducted a Lagrangian particle tracking in the Santa Barbara
123 Channel, CA, USA, using quadruple-nested high-resolution ROMS modeling with a
124 75-m horizontal grid size. Uchiyama *et al.* (2014) performed a Eulerian passive
125 tracer tracking for sewage outfalls in the Santa Monica and San Pedro bays in the
126 Southern California Bight using a similar quadruple-nested downscaling ocean
127 modeling. Both studies exhibited anisotropic along- and cross-shelf dispersal of
128 material concentrations and particles on the continental shelves and nearshore
129 areas, markedly dominated by submesoscale-eddy mixing. In addition to those
130 studies focusing on the eastern boundary currents, several other studies have
131 investigated the western boundary currents, such as the Kuroshio and its
132 extension region off Japan (*e.g.*, Sasaki *et al.*, 2014) and the Gulf Stream off the U.S.
133 east coast (*e.g.*, Gula *et al.*, 2014). However, the influence of submesoscale eddies on
134 upper-ocean dynamics and the resultant dispersal and transport of materials,
135 including the Kuroshio-derived warm water, nutrients, and coral larvae, has not yet
136 been investigated adequately around the Ryukyu Islands in the ECS.

137 Another important aspect of the Ryukyu Islands is their upheaved shallow
138 topography on the relatively deep Ryukyu Trough, which is situated on the eastern
139 side of the ECS continental shelf break where the Kuroshio persistently flows

140 northeastward. The islands obstruct the westward-propagating mesoscale eddies
141 that detach from the Kuroshio recirculation (Nakamura *et al.*, 2009). Therefore, this
142 obstruction may result in the emergence of unique turbulence such as island wakes
143 and associated eddy shedding, as has been investigated in the Southern California
144 Bight (*e.g.*, Dong and McWilliams, 2007). These geographical configurations are
145 presumed to set preferable conditions for the development of submesoscale-eddy
146 mixing through baroclinic and barotropic instability due to the Kuroshio fronts and
147 topographic shear within the study area.

148 In the present study, a submesoscale-eddy-resolving numerical
149 experiment was conducted for the area around the Ryukyu Islands. The study was
150 based on a double-nested ocean downscaling configuration using the ROMS,
151 embedded in the assimilative Japan Coastal Ocean Predictability Experiments
152 (JCOPE2) oceanic reanalysis (Miyazawa *et al.*, 2009) with atmospheric forcing from
153 the assimilative GPV-GSM (*e.g.*, Roads, 2004) and MSM (*e.g.*, Isoguchi *et al.*, 2010)
154 reanalysis products. The innermost ROMS model domain (the principal focus of this
155 analysis) had 1-km horizontal grid spacing, which was suitably fine for full
156 representation of submesoscale activities (Capet *et al.*, 2008). Particular attention
157 was given to the model's reproducibility, statistical description of intrinsic
158 submesoscale eddies, possible mechanisms for eddy inducement, and influence of
159 the eddies on the lateral mixing that promotes transport of the Kuroshio water
160 toward the islands. The remainder of this paper is organized as follows. A
161 description of the modeling framework used for the hindcast experiment for the
162 years 2010–2013 is given in Sec. 2. Section 3 illustrates an extensive comparison
163 between the model results and field observation and satellite altimetry data in order
164 to validate the model's capability of reproducing the Kuroshio and 3-D oceanic
165 structure. Section 4 considers the impact of downscaling, which is followed by
166 analyses of both the energy conversion and instability relevant to eddy kinetic
167 energy in Sec. 5 and of the heat flux in Sec. 6. Conclusions are given in Sec. 7

168

169 **2. Model configuration**

170

171 **Figure 1** shows the numerical domains of the oceanic downscaling model
172 in a double-nested configuration embedded in the JCOPE2 (Miyazawa *et al.*, 2009)
173 domain. The JCOPE2 is a numerical reanalysis product for the northwestern Pacific
174 Ocean assimilated with a vast amount of satellite and in situ data, including ARGO

175 floats using 3D-VAR. The JCOPE2 product is provided as daily averaged sea surface
176 height (SSH), temperature, salinity, and meridional and zonal horizontal current
177 velocities. We relied on a one-way offline nesting approach (Mason *et al.*, 2010) to
178 reduce the horizontal grid size from approximately 10 (JCOPE2) to 3 km
179 (ROMS-L1), and ultimately, down to 1 km (ROMS-L2). The parent ROMS domain
180 (ROMS-L1) had a horizontal size of 2304×2304 km with uniformly square 3-km
181 grid spacing and vertically stretched 32 σ -layers, designed to encompass a wide
182 area to consider all possible impacts of the Kuroshio flowing in from the Taiwan
183 Strait and the Luzon Strait. The climatological monthly freshwater discharge of the
184 Yangtze River into the ECS, which is reported to range approximately between
185 $838\text{--}907$ km³/yr (*e.g.*, Dai *et al.*, 2009), was taken into account. The innermost
186 ROMS-L2 domain was 832×608 km with 1-km horizontal resolution and 32
187 vertical σ -layers, which covered the entire chain of the Ryukyu Islands, from the
188 Amami Islands of Kagoshima Prefecture in the north to the Yaeyama Islands of
189 Okinawa Prefecture in the south. **Table 1** lists the numerical configuration of the
190 ROMS models.

191 The outermost boundary and initial conditions of ROMS-L1 were obtained
192 from the spatiotemporally interpolated fields of the daily averaged JCOPE2 data. The
193 model topography was obtained from the SRTM 30 Plus product (SRTM: Shuttle
194 Radar Topography Mission; Rodriguez *et al.*, 2005; Becker *et al.*, 2009), which
195 covers the global ocean at 30 geographic arc seconds, or roughly 1 km. We utilized
196 the QuikSCAT-ECMWF blended wind (*e.g.*, Bentamy *et al.*, 2006) for 2005–2007 and
197 the JMA GPV-GSM product (JMA: Japan Meteorological Agency, GPV-GSM: grid point
198 value of the Global Spectral Model) with horizontal resolution of $0.2^\circ \times 0.25^\circ$ for
199 2008–2013 for surface momentum forcing, depending on the availability of these
200 data sets. Surface heat, freshwater and radiation fluxes were taken from the COADS
201 (Comprehensive Ocean–Atmosphere Data Set; Woodruff *et al.*, 1987) monthly
202 climatology. The 20-day averaged JCOPE2 data were applied to the SST and sea
203 surface salinity (SSS) restoration with a time scale of 90 days to correct long-term
204 biases caused by the imposed climatological surface fluxes. The monthly
205 climatology of the major river discharges in Dai *et al.* (2009) was applied for the
206 Yangtze River. A four-dimensional TS nudging (a.k.a. robust diagnostic; *e.g.*,
207 Marchesiello *et al.*, 2003) with a weak nudging time scale of 1/20 per day was
208 applied to the 10-day averaged JCOPE2 temperature and salinity fields for
209 consistency of the Kuroshio path reproduced by the ROMS-L1 with that of JCOPE2.

210 The L1 model was used for more than eight years from January 1, 2005 until
211 September 14, 2013, UTC.

212 The innermost L2 model was initialized and forced along the boundary
213 perimeters by the spatiotemporally interpolated daily averaged L1 output. The
214 hourly output of the JMA GPV-MSM (Mesoscale Model) reanalysis, which
215 encompasses the entire L2 domain with horizontal resolution of $0.05^\circ \times 0.0625^\circ$,
216 was used for the L2 model instead of the GPV-GSM. Similar to the L1 model, SST and
217 SSS restoration for surface flux correction was included. The other numerical
218 conditions were the same as for the L1 model. Hence, the L2 model was run freely
219 without any assimilation such as the TS nudging that could interfere with the
220 spontaneous development and decay of intrinsic eddies. We note that the present
221 model does not include tidal forcing since it is considered to have minor effects on
222 mean and eddy field in such an open ocean configuration. For instance, Romero *et al.*
223 (2013) pointed out that dispersal and mixing in Santa Barbara Channel, CA, USA,
224 are dominated much prominently by submesoscale stirring, not by tides. The L2
225 model computational period was approximately 33 months, from December 27,
226 2010 to September 14, 2013, UTC. The statistical analyses conducted in the present
227 study exploit the model results for the same period between March 27, 2011 and
228 September 14, 2013, unless otherwise noted.

229

230 **3. Model Validation**

231

232 In this section, we compare the model results with satellite, in situ
233 observations, and the assimilative JCOPE2 reanalysis. **Figure 2** shows the time
234 series of the volume-averaged surface kinetic energy (KE) for the three model
235 results (*i.e.*, JCOPE2, ROMS-L1, and ROMS-L2). The volume average is taken over the
236 entire ROMS-L2 domain from the surface to a depth of 400 m, encompassing the
237 region in which the Kuroshio main body is most influential. The temporal variations
238 of the upper-ocean KE in the three models are similar. Given the fact that JCOPE2 is
239 assimilated with multiple satellite altimetry data, SST, ARGO, and in situ mooring
240 data, the two ROMS models provide realistic estimates of the near-surface eddy
241 activities. The ROMS-L2 generally yields slightly larger KE than the other cases
242 because it is a submesoscale eddy-resolving model that results in more energetic KE,
243 while retaining adequate seasonal variability. This result is achieved if the L1 model
244 is run with weak TS nudging toward the low-frequency JCOPE2 3-D density field, to

245 dissipate KE appropriately for realistic replication of the Kuroshio's behavior.
246 Otherwise, the KE in the L1 model increases significantly with unrealistically large
247 meandering of the Kuroshio path (not shown). Conversely, the L2 model with the
248 assimilated L1 boundary forcing behaves favorably, as shown in **Fig. 2**, without any
249 controls such as TS nudging.

250 Extensive model-data comparisons are performed using satellite altimetry
251 data and JMA observations to demonstrate the reproducibility of the double-nested
252 ROMS model. For validating the mean structure and temporal variance of the surface
253 currents, including the Kuroshio, we exploited the gridded composite of multiple
254 satellite altimetry data provided by AVISO (*e.g.*, Traon *et al.*, 1998). The delayed-time
255 AVISO-SSH data set is available daily with horizontal spacing of $1/4^\circ$. The magnitude
256 of the time-averaged geostrophic current velocity, estimated from the AVISO-SSH,
257 exhibits comparable magnitude with the corresponding patterns of the JCOPE2 and
258 ROMS-L2 on the L1 (**Fig. 3**). However, the Kuroshio intrusion into the South China
259 Sea from Luzon Strait in the ROMS-L1 model occurs more apparently than that in
260 AVISO and JCOPE2 where the westward meander is weakened with generating a
261 leaped eddy or a ring. The looping in the Luzon Strait could be realistic since it has
262 been reported both observationally and computationally (*e.g.*, Centurioni *et al.*,
263 2004 and Miyazawa *et al.*, 2004). Nevertheless, Luzon Strait is located sufficiently
264 far from the study area, and thus we conclude the plots of the ROMS velocity
265 magnitude also show reasonable agreement with the Kuroshio path of the other two
266 data sets. The SSH variance is viewed as a proxy that measures the intensity of the
267 temporal variability in synoptic and mesoscale signals mostly due to eddies and the
268 Kuroshio meanders. The ROMS-derived SSH variance reproduces several important
269 features with equivalent magnitudes to the AVISO data. For instance, the variance is
270 smaller on the persistent Kuroshio path on the western side of the Ryukyu Islands,
271 compared with the other side, where the westward-traveling Rossby waves and
272 mesoscale eddies collide with the topographic ridge around the islands. Another
273 energetic area commonly arises north of 29°N , off the southwest coast of Kyushu
274 Island.

275 The modeled stratification is subsequently compared with in situ
276 observations from the vertical section along the PN Line transect (*e.g.*, Miyazawa *et al.*
277 *et al.*, 2009), indicated by the thick black lines in **Fig. 1**. The PN Line measurements
278 comprise 16 CTD (conductivity, temperature and depth) casts that have been
279 obtained seasonally since 1972 by JMA research vessels. As this transect favorably

280 transverses the Kuroshio path in the ECS, we can estimate the volume transport
 281 across the PN Line. Comparisons of the seasonally averaged temperature and
 282 salinity clearly illustrate that the present model is capable of reproducing the
 283 observed stratification, not just in spring (**Fig. 4**) but in all seasons (not shown). A
 284 tilted thermocline and halocline are formed toward the ECS shelf region with
 285 subsurface salinity maxima in the trough region. **Table 2** summarizes the modeled
 286 and observed volume flux (transport) in Sverdrup along the PN Line. The observed
 287 volume fluxes are estimated geostrophically from the slope of the isobaric surface,
 288 based on the seasonal climatology of the temperature and salinity (**Fig. 4**) by
 289 assuming the transport vanishes at 1000 m depth. The volume fluxes obtained by
 290 the models principally contain the ageostrophic component, which results in slightly
 291 larger transport than those observed. However, the modeled volume fluxes
 292 adequately capture the observed seasonal variability, such as the increase in
 293 summer and the decrease in fall. Interestingly, the ROMS-L2, with the finest grid
 294 resolution without TS nudging, provides a better estimate of the transport
 295 (compared with the observations) than that evaluated using the coarser-resolution
 296 models (*viz.*, ROMS-L1 and JCOPE2), both of which employ data assimilation to some
 297 extent. This is likely attributable to the occurrence of an appropriate spontaneous
 298 flux adjustment in the ROMS-L2 through submesoscale lateral mixing and
 299 associated dissipation at the resolved scales of the mean KE around the Kuroshio
 300 path. In summary, the presented double-nested ROMS model is shown satisfactorily
 301 capable of reproducing the mesoscale behavior of the Kuroshio and the mean 3-D
 302 oceanic structure.

303 **4. Downscaling effects**

304

305 The unassimilated L2 model is capable of fully resolving submesoscale
 306 eddies, whereas the L1 and JCOPE2 are submesoscale-permitting (Capet *et al.*,
 307 2008). Therefore, eddy activity should be enhanced by the grid refinement of the
 308 downscaling via the increase and strengthening of the resolved eddies. To examine
 309 the downscaling effects, surface eddy kinetic energy (EKE), K_e , can be estimated as
 310 follows:

$$311 \quad K_e = \frac{1}{2} (\overline{u'^2 + v'^2}) , \quad (1)$$

312 where (u, v) is the horizontal velocity and the overbar represents an
313 ensemble-averaging operator. The variables assigned with the prime are the
314 fluctuating eddy components obtained by removing the seasonal variations with a
315 low-pass Butterworth filter in the frequency domain (the first and last 10% of the
316 analysis period cannot be used because of the Butterworth filter's properties).
317 **Figure 5a-c** demonstrates that the surface EKE increases markedly as the model
318 grid spacing decreases from 10 to 3 and to 1 km. The higher EKE mostly emerges in
319 two distinct regions: one is on the Kuroshio axis and the other is on its eastern side,
320 close to Okinawa (Main) Island.

321 **Figure 5d-f** illustrates the daily averaged, surface relative vorticity
322 normalized by the background rotation f (the Coriolis parameter), *viz.*, representing
323 the emergence of mesoscale and submesoscale eddies in each model. The variable
324 ζ/f is also known as the vortical Rossby number, the absolute value of which is
325 greater than unity when ageostrophy is more evident. Vorticity is generally
326 distributed as streaks and filaments around the Kuroshio axis where the change of
327 sign occurs. However, enclosed circular eddies are dominant away from the axis, in
328 particular, in the two ROMS model results. The two distinctive high EKE (K_e) regions
329 in **Fig. 5a-c** are consistent with these vorticity distributions. As the resolution
330 becomes finer, the extent and magnitudes of the resolved vortices become
331 prominently diversified and enhanced, coinciding with the high EKE region on the
332 eastern side of the Kuroshio (**Fig. 5a-c**). The higher-resolution model renders
333 smaller submesoscale eddies that typically have diameters of several kilometers.

334 We notice that negative vorticity, *viz.*, counter-clockwise-rotating cyclonic
335 eddies, develops more vigorously and widely on the east side of the Kuroshio than
336 on the other side, where positive vorticity dominates. The innermost model with the
337 highest resolution (ROMS-L2) captures the negative vorticity that is retained
338 significantly on the eastern side of the Kuroshio, while the centrifugally stable
339 positive vorticity is attenuated rather quickly there. The ROMS-L2 model has the
340 smallest eddies and the largest negative vorticity near the islands. This negative bias
341 near the islands, in the direction transverse to the Kuroshio path, is presumably
342 caused by the increase of the resolved eddies with the increased model resolution.
343 To confirm this negative bias quantitatively, the probability density function (PDF)
344 of the normalized relative vorticity (ζ/f) at the surface was determined as a function
345 of the westward transverse distance from Okinawa Island along transect AA', as
346 shown in **Fig. 5f**. This transect is defined normal to the mean Kuroshio axis,

347 averaged over the computational period, which is inclined at 35° relative to the
 348 geographical coordinate. **Figure 6** indicates that the finer-resolution models yield
 349 stronger vortices with gentler PDF slopes along the ordinates. Although the PDFs
 350 are distributed nearly symmetrically with respect to the Kuroshio axis, they peak at
 351 $\zeta/f < 0$ on the eastern side of the Kuroshio axis, even adjacent to Okinawa Island.
 352 This negative bias on the east is most evident at the highest resolution. On the west
 353 of the Kuroshio, large positive vorticity appears immediately next to the Kuroshio,
 354 while the PDF peaks converge to zero away from the axis to the west. In summary,
 355 the Ryukyu Islands are considered to enhance both intensity and fluctuations of the
 356 anticyclonic negative vorticity on the eastern side of the Kuroshio axis. However, on
 357 the other side, anticyclones and cyclones compete with the activated positive
 358 vorticity near the Kuroshio axis. This transverse asymmetry is a unique structure
 359 that characterizes the eddy field of the study area, which is perhaps related to both
 360 the topographic ridge near the island chain and the continental shelf break along
 361 which the Kuroshio persistently drifts (**Fig. 1**), as well as frontal processes
 362 associated with the Kuroshio warm water.

363

364 **5. Energy conversion analysis**

365

366 Energy conversion rates in the eddy kinetic energy (K_e) conservation
 367 equation are often used to quantify the relative importance of instability and
 368 eddy-mean interaction mechanisms (*e.g.*, Marchesiello *et al.*, 2003; Dong *et al.*,
 369 2006; Klein *et al.*, 2008). If the conversion of mean kinetic energy to eddy kinetic
 370 energy $K_m K_e$ (*viz.*, barotropic conversion rate) is positive, it implicates the
 371 occurrence of shear instability in the extraction of K_e to energize eddies. If the
 372 conversion of eddy potential energy to eddy kinetic energy $P_e K_e$ (*viz.*, baroclinic
 373 conversion rate) is positive, baroclinic instability is expected. We focus on these two
 374 primary quantities, as expressed in the following equations, in the investigation of
 375 the stimulation mechanisms of K_e :

$$376 \quad K_m K_e = -\left(\overline{u'u'} \frac{\partial u}{\partial x} + \overline{u'v'} \frac{\partial u}{\partial y} + \overline{u'w'} \frac{\partial u}{\partial z} + \overline{v'u'} \frac{\partial v}{\partial x} + \overline{v'v'} \frac{\partial v}{\partial y} + \overline{v'w'} \frac{\partial v}{\partial z}\right), \quad (2)$$

$$377 \quad P_e K_e = -\frac{g}{\rho_0} \overline{\rho'w'}, \quad (3)$$

378 where (x, y, z) are the horizontal and vertical coordinates, w is the vertical velocity, ρ
379 is the density of sea water, $\rho_0 = 1027.5 \text{ kgm}^{-3}$ is the Boussinesq reference density,
380 and g is gravitational acceleration. The vertically integrated $K_m K_e$, $P_e K_e$, and K_e (EKE)
381 over the mixed layer from the ROMS-L2 model are plotted in **Fig. 7a-c**. The
382 averaged mixed-layer depth estimated by the KPP model (Large *et al.*, 1994) used in
383 the ROMS is approximately 50 m in the L2 domain. The mixed-layer integrated $P_e K_e$
384 is positive almost everywhere with two distinctly high regions around the Kuroshio
385 axis and the neighboring flank on the eastern side to the islands (**Fig. 7b**). This $P_e K_e$
386 distribution illustrates the importance of baroclinic instability in the vorticity
387 generation within these two regions. In contrast, an axisymmetric pair of large
388 positive and negative areas of $K_m K_e$ can be observed in the narrow strips on both
389 sides of the Kuroshio, representing the lateral shear instability induced by the
390 Kuroshio (**Fig. 7a**). In general, the regions with positive $P_e K_e$ and positive $K_m K_e$
391 coincide with the areas of high K_e (**Fig. 7c**).

392 The area of highly positive $P_e K_e$ is distributed widely between the
393 Kuroshio path and the Ryukyu Islands, whereas the highly positive $K_m K_e$ appears
394 mostly near the Kuroshio and on the western side of the islands near the
395 topography. The vertically integrations of $K_m K_e$, $P_e K_e$, and K_e over the mixed layer
396 along the transect are plotted in **Fig. 8**. Consistent with **Fig. 7a-c**, $P_e K_e$ is positive
397 and larger than $K_m K_e$ almost everywhere along the transect, indicating that
398 baroclinic instability is the dominant mechanism for eddy generation near the
399 surface, especially, on the eastern side of the Kuroshio path where high values of K_e
400 appear. Therefore, it is manifest that the negative vorticity on the eastern side of the
401 Kuroshio (**Fig. 5f**) is provoked by a combination of the lateral shear affected by the
402 Kuroshio, topographic eddy shedding near the islands, and baroclinic instability due
403 to the Kuroshio front. The negative $K_m K_e$ on the western side of the Kuroshio
404 suggests that positive vorticity is suppressed by the lateral shear through an inverse
405 energy cascade while baroclinically destabilized by the competing positive $P_e K_e$.

406 The EKE (K_e) budget is examined further for the subsurface water, where
407 the Kuroshio is influential, by vertical integration of $K_m K_e$, $P_e K_e$, and K_e from the
408 surface down to a depth of 1200 m with the L2 result (**Fig. 7d-f**). The L2 model
409 detects large positive barotropic and baroclinic conversion rates near the Kuroshio
410 that coincide with the region of high K_e . In addition, an increase of the subsurface
411 $P_e K_e$ and resultant intensification of K_e are evident on the eastern side of the islands,
412 due to a branch of the Kuroshio known as the *Ryukyu (Under) Current* (e.g., Kawabe,

413 2001; Andres *et al.*, 2008). This large $PeKe$ could induce further subsurface
414 westward lateral mixing and intrusion of the Ryukyu Current. However, this is
415 beyond the scope of the present study and it will be examined elsewhere. The
416 subsurface structure on the western side of the islands is illustrated in **Fig. 9** with
417 respect to the vertical cross-section along transect AA' (see **Fig. 5f**). The Kuroshio
418 main body is inclined on the shelf slope with a mean streamwise velocity of >0.2
419 m/s, even at 600 m depth. High Ke is distributed widely near the surface to the east,
420 coinciding with the positive $KmKe$ near the Kuroshio and positive $PeKe$ extending
421 between the Kuroshio and Okinawa Island. Conversely, high Ke is mostly confined
422 along the shelf break from the surface to 400 m depth to the west, where both $KmKe$
423 and $PeKe$ increase in magnitude with the sign change.

424 Below the mixed layer, the Kuroshio is squeezed strongly against the shelf
425 slope on the eastern side, which provokes large velocity shear and thus large
426 positive $KmKe$, which is associated with the shear instability due to topographic eddy
427 shedding. Around the inclined Kuroshio core, competing large positive $PeKe$ and
428 large negative $KmKe$ are formed simultaneously below the mixed layer down to a
429 depth of 600 m. **Figure 10** shows a snapshot of the daily averaged, normalized
430 relative vorticity (ζ/f) field in the vertical section along the transect and in the
431 horizontal section at $z = -400$ m from the L2 model. In **Fig. 10a**, negative vorticity
432 (anticyclonic submesoscale eddies) appears dominantly near the surface on the
433 eastern side of the Kuroshio toward Okinawa Island, while positive cyclonic vorticity
434 appears around the Kuroshio core from the surface down to depths beyond 500 m
435 along the shelf slope. The diameter of this cyclone is approximately 50 km, which
436 still fits within a typical submesoscale range. In **Fig. 10b**, cyclonic eddy shedding
437 occurs quasi-periodically from the shelf slope topography. Therefore, a combination
438 of topographic shear and baroclinic instability promotes the near-surface
439 anticyclonic eddies and subsurface cyclonic eddies, both of which are submesoscale.

440

441 **6. Heat flux analysis**

442

443 The submesoscale anticyclonic eddies induced by the Kuroshio are
 444 anticipated to promote eastward material transport to the west coast of Okinawa
 445 Island through lateral eddy mixing. To quantify this effect, we assessed the lateral
 446 turbulent mixing of a tracer (*i.e.*, heat) in the upper ocean. The time-averaged,
 447 vertically integrated heat (potential temperature) transport equation is
 448 represented as (*e.g.*, Marchesiello *et al.*, 2003):

$$449 \int_{-h}^{\eta} \left(\frac{\partial uT}{\partial x} + \frac{\partial vT}{\partial y} \right) dz + \int_{-h}^{\eta} \left(\frac{\partial u'T'}{\partial x} + \frac{\partial v'T'}{\partial y} \right) dz + \int_{-h}^{\eta} [Q(\bar{T}) + D(\bar{T})] dz = 0, \quad (4)$$

450 where T is potential temperature, Q is the sea surface heat flux, D is the
 451 parameterized vertical and horizontal subgrid-scale mixing of heat, h is depth, and η
 452 is surface elevation. We focus on the advective transport by eddying flow, which is a
 453 divergence of lateral eddy heat fluxes (EHFs) \mathbf{F} :

$$454 \mathbf{F} = (F_x, F_y) = (\rho_{ll} C_p \overline{u'T'}, \rho_{0l} C_p \overline{v'T'}) , \quad (5)$$

455 where $C_p = 4000 \text{ Jkg}^{-1}\text{C}^{-1}$, which is the heat capacity of seawater at a constant
 456 pressure. To quantify the eddy heat transport to the islands, a divergent component
 457 of the EHF is evaluated. The EHF can be decomposed into divergent and rotational
 458 components using Helmholtz's theorem (*e.g.*, Aoki *et al.*, 2013) such that

$$459 \mathbf{F} = \mathbf{k} \times \nabla\psi + \nabla\varphi \equiv \text{rEHF} + \text{dEHF}, \quad (6)$$

460 where \mathbf{k} is a vertical unit vector, and ψ and φ are scalar quantities similar to a
 461 streamfunction and a velocity potential, respectively. We introduce the notation
 462 where rEHF and dEHF are the rotational and divergent components of the EHF. This
 463 decomposition is conducted by numerically solving the Poisson equation (6) with
 464 Neumann boundary conditions.

465 The mixed-layer integrated EHF, rEHF, and dEHF vectors, superimposed
 466 on their transverse component relative to the mean Kuroshio path from the L2
 467 result, are plotted in **Fig. 11a–c**. The total EHF (**Fig. 11a**) is properly decomposed
 468 into the rEHF (**Fig. 11b**) and dEHF (**Fig. 11c**). The rEHF vectors mainly follow the
 469 prevailing direction of the northeastward-drifting Kuroshio path with recurring
 470 southwestward eddy heat transport near the islands. The eddy heat transport in the

471 opposite direction to the Kuroshio near the islands is obviously due to a mesoscale
472 secondary circulation often known as the *Kuroshio Counter Current*, as reported in
473 previous studies (*e.g.*, Qiu and Imasato, 1990). However, the mixed-layer integrated
474 dEHF properly measures the contribution normal to the Kuroshio axis, which
475 manifests the lateral eddy heat transport toward the islands. **Figure 11c** also
476 demonstrates that the near-surface heat transport to the islands occurs more
477 strongly on the eastern side of the Kuroshio, although a weaker northwestward heat
478 transport occurs on the other side. This near-surface heat transport toward the
479 islands is obviously induced by anticyclonic submesoscale eddies developed around
480 the Ryukyu Islands (**Sec. 4**).

481 **Figure 11d-f** shows the vertically integrated EHF vectors from the
482 surface to 1200 m depth. In general, the vectors are similar to those integrated over
483 the mixed layer, although several substantial differences can be observed. The total
484 EHF and rEHF occurs mainly in the direction of the Kuroshio path, whereas the
485 major transport bifurcates around Ishigaki Island, which is located near the
486 lower-left corner of the domain, forming the Ryukyu Current EHF branch that
487 passes on the eastern side of Okinawa Island. As this subsurface branch drifts close
488 to several islands, including Okinawa Island, the influence of the Kuroshio on the
489 Ryukyu Islands is partially brought by this under current. Other differences include
490 the attenuated positive across-Kuroshio transport (dEHF) between the Kuroshio
491 and Okinawa Island and the southeastward subsurface dEHF on the eastern side of
492 the islands due to the Ryukyu Current. These findings illustrate that the
493 near-surface dEHF brings the Kuroshio warm water to the islands, whereas the
494 subsurface dEHF affects them in a different way.

495 **Figure 12** shows cross-sectional plots of mean temperature, temperature
496 variance, and dEHF (eastward positive to Okinawa Island) along the transect. The
497 mean thermocline and mixed-layer depths become shallower toward the ECS shelf
498 from Okinawa Island. However, the Kuroshio induces additional effects such that the
499 mean thermocline is inclined to shallow both toward the ECS shelf and toward
500 Okinawa Island, with a near-surface bulge of warm water around the Kuroshio axis.
501 The maximum lateral temperature gradient is formed adjacent to the Kuroshio core
502 that is inclined on the shelf slope. The overall stratification is increased by this
503 inclined thermocline, established from the thermal wind relation with the
504 cross-sectional velocity structure due to the Kuroshio. Although the across-Kuroshio
505 dEHF is positive and confined mostly in the mixed layer in the east, a tongue of

506 negative dEHF is formed in the west, which penetrates to a depth of 400 m along
507 the slope (**Fig. 12c**). The temperature variance (**Fig. 12b**) is large where the dEHF
508 and K_e (see **Fig. 8c**) are consistently large. Interestingly, the temperature variance is
509 increased around the mean mixed-layer depth on the ECS shelf, perhaps provoked
510 by temporal fluctuations of the thermocline.

511 The mixed-layer integrated dEHF along the transect (**Fig. 13**) indicates
512 that energetic lateral eddy heat transport is induced within and around the surface
513 mixed layer, leading to the zonal transport of the Kuroshio warm water. The positive
514 eddy flux develops more strongly on the eastern side of Kuroshio than does the
515 negative flux on the other side in the mixed layer. Nevertheless, the largest
516 temperature variance emerges between the Kuroshio and the slope where the
517 tongue of negative dEHF exists. The subsurface topographic eddy shedding on the
518 slope (**Fig. 10**) promotes this tongue of negative dEHF, which results in subsurface
519 westward heat transport via the warm water brought up from the bottom of the
520 Kuroshio to the ECS shelf. As a consequence of all these processes, lateral eddy heat
521 transport occurs asymmetrically relative to the Kuroshio path.

522

523

524 **7. Conclusions**

525

526 Eddy-induced lateral mixing due to the Kuroshio around the Ryukyu
527 Islands in the ECS was investigated using a double-nested ROMS model that
528 downscales the assimilative JCOPE2 oceanic reanalysis to the innermost
529 submesoscale eddy-resolving model with 1-km grid spacing. An extensive
530 model-data comparison was performed against field observations and satellite
531 altimetry data to demonstrate the model's capability of reproducing the Kuroshio
532 and 3-D oceanic structure. The model-data comparison demonstrated that the
533 elaborated innermost high-resolution ROMS-L2 model successfully reproduced
534 mesoscale structures spontaneously without any data assimilation.

535 The L2 models simulated significant negative vorticity bias, comprising
536 anticyclonic mesoscale and submesoscale eddies, on the western side of the islands.
537 The PDF of the normalized relative vorticity along the transect normal to the mean
538 Kuroshio path supported this asymmetric appearance of negative vorticity. Positive
539 vorticity was confined mostly to the vicinity of the Kuroshio, while the peak vorticity
540 PDF converged to zero (*viz.*, almost no positive and negative bias) toward the ECS

541 shelf. These results reinforce the speculation that eddies are generated because of
542 interactions between the Kuroshio warm water and the unique local topography,
543 including the ridge of the islands to the east and the ECS continental shelf break to
544 the west, along which the Kuroshio persistently flows.

545 The energy conversion analysis focusing on the barotropic and baroclinic
546 conversion rates suggested that the near-surface anticyclonic negative vorticity on
547 the eastern side of the Kuroshio and the subsurface cyclonic positive vorticity on the
548 western side are generated via the combination of shear instability and baroclinic
549 instability, both of which are evidently influenced by the Kuroshio. Conversely, the
550 negative barotropic conversion rate, which appeared near the Kuroshio axis,
551 suggested that cyclonic positive vorticity is suppressed by the Kuroshio's lateral
552 shear near the surface. The resultant surface EKE is thus also asymmetric with
553 respect to the Kuroshio, with greater EKE distributed widely on the eastern side of
554 the path. However, the subsurface water below the mixed layer reflected a
555 pronouncedly different energy balance. The magnitude of the subsurface barotropic
556 conversion rate is large on the shelf break, where a positive conversion rate
557 appears near the slope, whereas a negative rate appears to the east, where it
558 competes with a large positive baroclinic conversion rate.

559 The heat flux analysis solidly explained that these eddies promote lateral
560 material transport from the Kuroshio. Helmholtz decomposition was introduced to
561 the EHF to evaluate the rotational and divergent components of the EHF, rEHF, and
562 dEHF. The decomposed rEHF detected the contribution from the EHF that mainly
563 follow the Kuroshio and the anticyclonic recurring secondary circulation referred to
564 as the *Kuroshio Counter Current*. Conversely, the dEHF measured the contribution
565 normal to the Kuroshio axis, which represents the transverse eddy-induced
566 transport to the islands. The surface lateral eddy heat transport occurs
567 asymmetrically relative to the Kuroshio axis, with greater transverse eastward
568 transport than toward the ECS shelf. This occurs because of the more energetic
569 anticyclonic submesoscale eddies on the eastern side of the Kuroshio. Consistent
570 with the subsurface energy conversion rates, the depth-integrated EHF were
571 visibly different from those near the surface. Although the depth-integrated EHF
572 and rEHF occur mainly in the direction of the Kuroshio path, the across-Kuroshio
573 transport (*viz.*, dEHF) showed that they can be enhanced significantly near the
574 surface, which promotes warm water transport in both transverse directions
575 relative to the Kuroshio path. However, a “negative dEHF tongue” was found to form

576 uniquely on the shelf slope and thus the subsurface warm water is brought upward
577 along the slope toward the ECS shelf. This negative dEHF tongue was attributed to
578 subsurface eddies generated by a combination of the baroclinic and shear instability,
579 according to the energy conversion analysis. These subsurface eddies are evidently
580 shed on the ECS shelf slope down to a depth of 600 m as energetic cyclonic
581 submesoscale eddies.

582 The present study clarified that the Kuroshio warm water undoubtedly
583 influences the biologically diverse ecosystems with abundant corals that have
584 formed around the Ryukyu Islands through mechanical intrusion. Based on the
585 modeling results, it was established that the Kuroshio-derived waters approach the
586 islands in at least three ways: 1) by transverse eddy-induced lateral mixing near the
587 surface, 2) via a clockwise recurring flow known as the *Kuroshio Counter Current*,
588 and 3) via a subsurface pathway associated with the *Ryukyu Current*. This study
589 focused primarily on the first mechanism that is accompanied by subsurface
590 submesoscale eddy transport toward the ECS shelf, induced by topographic eddy
591 shedding on the slope. Further analysis will be required to elucidate the detailed
592 mechanisms leading to the other two processes.

593

594 **Acknowledgements**

595 We are grateful to James C. McWilliams, Alexander F. Shchepetkin, and M.
596 Jeroen Molemaker of UCLA and Mayumasa Miyazawa of JAMSTEC for their help and
597 comments on the numerical modeling. We are also grateful to Shohei Nakada of
598 OIST for his help on the organizing JMA's research vessels data. This study was
599 supported by JSPS Grant-in-Aid for Scientific Research C and B (KAKENHI grant
600 numbers: 24560622 and 15H04049).

601

602 **References**

603

- 604 1) Andres, M., Park, J., Wimbush, M., Zhu, X., Chang, K. and Ichikawa, H. 2008. Study
605 of the Kuroshio/Ryukyu Current System Based on Satellite-Altimeter and in situ
606 Measurements. *J. Oceanogr.*, **64**, 937-950.
- 607 2) Aoki, K., Minobe, S., Tanimoto, Y. and Sasai, Y. 2013. Southward Eddy Heat
608 Transport Occurring along Southern Flanks of the Kuroshio Extension and the
609 Gulf Stream in a 1/108 Global Ocean General Circulation Model. *J. Phys. Oceanogr.*,

- 610 **43**, 1899-1910.
- 611 3) Badin, G., Tandon, A. and Mahadevan, A. 2011. Lateral Mixing in the Pycnocline
612 by Baroclinic Mixed Layer Eddies. *J. Phys. Oceanogr.*, **41**, 2080-2101.
- 613 4) Becker, J. J., Sandwell, D. T., Smith, W. H. F., Braud, J., Binder, B., Depner, J., Fabre,
614 D., Factor, J., Ingalls, S., Kim, S-H., Ladner, R., Marks, K., Nelson, S., Pharaoh, A.,
615 Trimmer, R., Von Rosenberg, J., Wallace, G. and Weatherall, P. 2009. Global
616 Bathymetry and Elevation Data at 30 Arc Seconds Resolution: SRTM30_PLUS,
617 *Marine Geodesy*, **32:4**, 355-371.
- 618 5) Bentamy, A., Ayina, H.-L., Queffeuilou, P., and Croize-Fillon, D. 2006, Improved
619 near real time surface wind resolution over the Mediterranean Sea. *Ocean
620 Science Discussions*, **3 (3)**, pp.435-470.
- 621 6) Blumberg, A. F. and G. L. Mellor, 1987. A description of a three-dimensional
622 coastal ocean circulation model. In: *Three-Dimensional Coastal ocean Models*.
623 Coastal and estuarine sciences: Volume 4, Ed: N. Heaps, Ameri. Geophys. Union,
624 Washington, D.C., USA, 1-16.
- 625 7) Boccaletti, G., Ferrari, R. and Fox-Kemper, B. 2007. Mixed Layer Instabilities
626 and Restratification. *J. Phys. Oceanogr.*, **37**, 2228-2250.
- 627 8) Callies, J., Ferrari, R., Klymak, J. M. and Gula, J. 2015. Seasonality in submesoscale
628 turbulence, *Nature Comm.*, **6**, Article number: 6862.
- 629 9) Capet, X., McWilliams, J.C., Molemaker, J.M. and Shchepetkin. A.F. 2008.
630 Mesoscale to Submesoscale Transition in the California Current System. Part I:
631 Flow Structure, Eddy Flux, and Observational Tests. *J. Phys. Oceanogr.*, **38**, 29-43.
- 632 10) Capet, X., McWilliams, J.C., Molemaker, J.M. and Shchepetkin. A.F. 2008.
633 Mesoscale to Submesoscale Transition in the California Current System. Part II:
634 Frontal Processes. *J. Phys. Oceanogr.*, **38**, 44-64
- 635 11) Capet, X., McWilliams, J.C., Molemaker, J.M. and Shchepetkin. A.F. 2008.
636 Mesoscale to Submesoscale Transition in the California Current System. Part III:
637 Energy Balance and Flux. *J. Phys. Oceanogr.*, **38**, 2256-2269.
- 638 12) Cesar, H.J.S., Burke, L., and Pet-Soede, L., 2003. *The Economics of Worldwide Coral
639 Reef Degradation*. Cesar Environmental Economics Consulting, Arnhem, and
640 WWF-Netherlands, Zeist, The Netherlands. 23pp.

- 641 13) Centurioni, L.R., Niiler, P.P. and Lee, D.K. 2004 Observations of Inflow of
642 Philippine Sea Surface Water into the South China Sea through the Luzon Strait.
643 *J. Phys. Oceanogr.*, **34**, 113–121.
- 644 14) Dai, A., Qian, T., Trenberth, K.E. and Milliman, J.D. 2009. Changes in continental
645 freshwater discharge from 1948-2004, *J. Climate*, **22**, 2773-2791.
- 646 15) Dong, C., McWilliams, J.C. and Shchepetkin, A.F. 2006. Island Wakes in Deep
647 Water, *J. Phys. Oceanogr.*, **37**, 962–981.
- 648 16) Dong, C. and McWilliams, J.C. 2007. A numerical study of island wakes in the
649 Southern California Bight. *Cont. Shelf Res.*, **27**, 1233–1248.
- 650 17) Gula, J., Molesmaker, M.J. and McWilliams, J.C. 2014. Submesoscale Cold Filaments
651 in the Gulf Stream. *J. Phys. Oceanogr.*, **44**, 2617-2643.
- 652 18) Guo, X., Hukuda, H., Miyazawa, Y. and Yamagata, T. 2003, A Triply Nested Ocean
653 Model for Simulating the Kuroshio --- Roles of Horizontal Resolution on JEBAR. *J.*
654 *Phys. Oceanogr.*, **33**, 146-169.
- 655 19) Ichikawa, H. and Beardsley, R. C., 1993. Temporal and spatial variability of
656 volume transport of the Kuroshio in the East China Sea. *Deep-Sea Res. I*, **40**,
657 583–605.
- 658 20) Ichikawa, H. and Chaen, M., 2000. Seasonal variation of heat and freshwater
659 transports by the Kuroshio in the East China Sea. *J. Mar. Sys.*, **24**, 119–129.
- 660 21) Imawaki, S., Uchida, H., Ichikawa, H., Fukazawa, M., Umatani, S., and the ASUKA
661 Group, 2001. Satellite altimeter monitoring the Kuroshio transport south of
662 Japan. *Geophys. Res. Lett.*, **28 (1)**, 17–20.
- 663 22) Isoguchi, O., Shimada, M. and Kawamura, H. 2010. Characteristics of Ocean
664 Surface Winds in the Lee of an Isolated Island Observed by Synthetic Aperture
665 Radar. *Mon. Wea. Rev.*, **139**, 1744-1761.
- 666 23) Johns, W. E., Lee, T. N., Zhang, D. and Zantopp, R. 2001. The Kuroshio East of
667 Taiwan: Moored transport observations from the WOCE PCM-1 Array. *J. Phys.*
668 *Oceanogr.*, **31**, 1031–1053.
- 669 24) Kawabe, M. 2001. Interannual variations of sea level at Nansei Islands and
670 volume transport of the Kuroshio due to wind changes. *J. Phys. Oceanogr.*, **57**,
671 189–205.

- 672 25) Klein, P., Hua, B.-L., Lapeyre, G., Capet, X., Le Gentil, S. and Sasaki, H. 2008.
673 Upper ocean turbulence from high-resolution 3D simulations. *J. Phys. Oceanogr.*,
674 **38**, 1748-1763.
- 675 26) Kunze, E., Klymak, J.M., Lien, R.-C., Ferrari, R., Lee, C.M., Sundermeyer, M.A. and
676 Goodman, L. 2015. Submesoscale Water-Mass Spectra in the Sargasso Sea. *J.*
677 *Phys. Oceanogr.*, **45**, 1325–1338.
- 678 27) Large, W. G., McWilliams, J.C., and Doney, S. C. 1994. Oceanic Vertical mixing: a
679 review and model with a nonlocal boundary layer parameterization, *Rev.*
680 *Geophys.*, **32**, 363–403.
- 681 28) Marchesiello, P., McWilliams, J.C. and Shchepetkin, A. 2003. Equilibrium structure
682 and dynamics of the California Current System. *J. Phys. Oceanogr.*, **33**, 753–783.
- 683 29) Mason, E., Molemaker, J., Shchepetkin, A.F., Colas, F., McWilliams, J.C. and
684 Sangrà, P. 2010. Procedures for offline grid nesting in regional ocean models.
685 *Ocean Modelling.*, **35**, 1–15.
- 686 30) Miyazawa, Y., Guo, X. and Yamagata, T. 2004 Roles of Mesoscale Eddies in the
687 Kuroshio Paths. *J. Phys. Oceanogr.*, **34**, 2203–2222.
- 688 31) Miyazawa, Y., Zhang, R., Guo, X., Tamura, H., Ambe, D., Lee, J., Okuno, A., Yoshinari,
689 H., Setou, T. and Komatsu, K. 2009. Water Mass Variability in the Western North
690 Pacific Detected in 15-Year Eddy Resolving Ocean Reanalysis. *J. Oceanogr.*, **65**,
691 737–756.
- 692 32) Nadaoka, K., Nihei, Y., Wakaki, K., Kumano, R., Kakuma, S., Moromizato, S., Omija,
693 T., Iwao, K., Shimike, K., Taniguchi, H., Nakano, Y. and Ikema, T. 2001. Regional
694 variation of water temperature around Okinawa coasts and its relationship to
695 offshore thermal environments^[1] and coral bleaching. *Coral Reefs*, **20**, 373-384.
- 696 33) Nakamura, H., Nonaka, M. and Sasaki, H. 2009. Seasonality of the Kuroshio Path
697 Destabilization Phenomenon in the Okinawa Trough: A Numerical Study of Its
698 Mechanism. *J. Phys. Oceanogr.*, **40**, 530-550.
- 699 34) Penven, P., Debreu, L., Marchesiello, P. and McWilliams, J.C. 2006. Evaluation
700 and application of the ROMS 1-way embedding procedure to the California
701 Current Upwelling System. *Ocean Modell.*, **12**, 157–187.
- 702 35) Qiu, B. and Imasato, N. 1990. A numerical study on the formation of the
703 Kuroshio Counter Current and the Kuroshio Branch Current in the East China

- 704 Sea. *Cont. Shelf Res.*, **10**, 165-184
- 705 36)Qiu, B., 2001. Kuroshio and Oyashio Currents. In: *Encyclopedia of Ocean Sciences*,
706 Academic Press, 1413-1425.
- 707 37)Roads, J. 2004. Experimental Weekly to Seasonal U.S. Forecasts with the
708 Regional Spectral Model. *Bull. Amer. Meteor. Soc.*, **85**, 1887-1902.
- 709 38)Rodriguez, E., Morris, C.S. Belz, J.E., Chapin, E.C., Martin, J.M., Daffer, W. and
710 Hensley, S. 2005. An assessment of the SRTM topographic products. *Technical*
711 *Report JPL D-31639*, Jet Propulsion Laboratory, Pasadena, California, 143 pp.
- 712 39)Romero, L., Uchiyama, Y., Ohlman, J.C., McWilliams, J.C. and Siegel, D.A. 2013.
713 Simulations of Nearshore Particle-Pair Dispersion in Southern California. *J. Phys.*
714 *Oceanogr.*, **443**, 1862–1879.
- 715 40)Sasaki, H., Klein, P., Qiu, B. and Sasai, Y. 2014. Impact of oceanic-scale
716 interactions on the seasonal modulation of ocean dynamics by the atmosphere.
717 *Nature Comm.*, **5**, Article number: 5636.
- 718 41)Sasaki, Y., Minobe, S. and Inatsu, M. 2012. Influence of the Kuroshio in the East
719 China Sea on the Early Summer (Baiu) Rain. *J. Climate*, **25**, 6627–6645.
- 720 42)Shchepetkin, A.F. and McWilliams, J.C. 2005, The regional ocean modeling
721 system (ROMS): a split-explicit, free-surface, topography-following-coordinate
722 oceanic model, *Ocean Modell.*, **9**, 347–404.
- 723 43)Shchepetkin, A.F., McWilliams, J.C., 2008. Computational kernel algorithms for
724 fine- scale, multiprocess, longtime oceanic simulations. In: Temam, R., Tribbia, J.
725 (Eds.), *Handbook of Numerical Analysis*. Elsevier, Amsterdam, 119–181.
- 726 44)Spalding, M.D., Ravilious, C., Green, E.P., 2001. *World Atlas of Coral Reefs*. The
727 UNEP-World Conservation Monitoring Centre, University of California Press,
728 Berkeley, USA, 432 pp.
- 729 45)Traon, P.Y.L., Nadal, F. and Ducet, N. 1998. An Improved Mapping Method of
730 Multisatellite Altimeter Data. *J. Atmos. Oceanic Technol.*, **15**, 522-534.
- 731 46)Uchiyama, Y., Idica, E.Y., McWilliams, J.C. and Stolzenbach K.D. 2014.
732 Wastewater effluent dispersal in Southern California Bays. *Cont. Shelf Res.*, **76**,
733 36-52.
- 734 47)Usui, N., Ishizaki, S., Fujii, Y., Tsujino, H., Yasuda, T. and Kamachi, M. 2006.

- 735 Meteorological Research Institute Multivariate Ocean Variational Estimation
736 (MOVE) system: Some early results, *Advances in Space Research*, **37**, 806–822.
- 737 48) Usui, N., Tsujino, H., Fujii, Y. and Kamachi, M. 2008. Generation of a trigger
738 meander for the 2004 Kuroshio large meander. *J. Geophys. Res.*, **113**, C01012.
- 739 49) Woodruff, S.D., Slutz, R.J., Jenne, R.L. and Steurer, P.M. 1987. A Comprehensive
740 Ocean-Atmosphere Data Set. *Bull. Amer. Meteor. Soc.*, **68**, 1239-1250.
- 741 50) Xu, H., Xu, M., Xie, S. and Wang, Y. 2011. Deep atmospheric response to the
742 spring Kuroshio Current over the East China Sea. *J. Climate*, **24**, 4959–4972.
- 743 51) Yang, D., Yin, B., Liu, Z. and Feng, X. 2011. Numerical study of the ocean
744 circulation on the East China Sea shelf and a Kuroshio bottom branch northeast
745 of Taiwan in summer. *J. Geophys. Res.*, **116**, C05015.

Figure captions

Fig. 1 Double-nested ROMS model domains and bathymetry (color: m). Left: the

ROMS-L1 and L2 domains embedded in the JCOPE2 domain. Right: a zoomed-in region of the ROMS-L2 domain. Black thick line indicates the JMA PN Line transect.

Fig. 2 Time series of the volume-averaged surface ($z > -400$ m) kinetic energy from the ROMS-L1 (red), ROMS-L2 (blue), and JCOPE2 (black) models. The abscissa indicates the elapsed time in days since December 27, 2010, UTC.

Fig. 3 Plan view plots of: (a) time-averaged surface velocity magnitude and (b) SSH variance. Top: AVISO data, middle: JCOPE2, and bottom: ROMS-L2 on L1.

Fig. 4 Seasonally averaged temperature (left) and salinity (right) for spring from JMA observations (upper panels) and ROMS-L2 (lower panels) in the vertical section along the PN Line.

Fig. 5 Left panels—surface eddy kinetic energy (EKE), K_e , from: (a) JCOPE2, (b) ROMS-L1, and (c) ROMS-L2. Right panels—instantaneous spatial distributions of surface vorticity normalized by planetary vorticity, ζ/f (dimensionless) on January 7, 2012 from: (d) JCOPE2, (e) ROMS-L1, and (f) ROMS-L2. The black line in (f) indicates transect AA' for the cross-sectional plots.

Fig. 6 Probability density functions of the normalized relative vorticity at 2 m depth along transect AA' (see **Fig. 5f**) from: (a) JCOPE2, (b) ROMS-L1, and (c) ROMS-L2 models, as a function of distance from Okinawa Island (km). The black lines are the mean Kuroshio axes.

Fig. 7 Left panels: (a) barotropic conversion rate, $K_m K_e$, (b) baroclinic conversion rate, $P_e K_e$, and (c) EKE, K_e , integrated vertically over the mixed layer from the ROMS-L2 model results. Right panels: same as the left panels, but integrated vertically from the surface down to 1200 m depth. The gray contours represent surface velocity magnitude >0.5 m/s with intervals of 0.25 m/s.

Fig. 8 Vertically integrated $K_m K_e$ (red thin line), $P_e K_e$ (red thick line) and K_e (blue line) over the mixed layer from ROMS-L2 along the transect shown by the black line in **Fig. 5f**. The black line indicates the mean position of the Kuroshio axis.

Fig. 9 Cross-sectional plots of: (a) barotropic conversion rate, $K_m K_e$, (b) baroclinic conversion rate, $P_e K_e$, and (c) EKE, K_e , from the ROMS-L2 model. The corresponding transect is shown by the black line in **Fig. 5f**. The white lines are the mean mixed-layer depth estimated from the KPP model in ROMS. The black contours represent the mean streamwise velocity normal to the transect.

Fig. 10 (a) Cross-sectional plot of normalized relative vorticity ζ/f on January 7, 2012, along transect AA' (shown by the black line in **Fig. 5f**). The white line is the mixed-layer depth estimated from the KPP model. (b) Normalized relative vorticity ζ/f in the horizontal plane at $z = -400$ m on January 7, 2012.

Fig. 11 Eddy heat flux (EHF) vectors vertically integrated (left) over the mixed layer and (right) from the surface to depth of 1200 m, superposed on the across-Kuroshio component of the labeled EHF (in color). (upper) total EHF, (middle) rotational component, rEHF, and (lower) divergent component, dEHF. The gray contours are surface velocity magnitude >0.5 m/s with intervals of 0.25 m/s.

Fig. 12. Cross-sectional plots of: (a) mean streamwise velocity normal to the transect (contours) and mean temperature (color), (b) temperature variance, and (c) across-Kuroshio component of the divergent eddy heat flux, dEHF (eastward positive toward the islands) from the ROMS-L2 results, along the transect shown by the black line in **Fig. 5f**. White line shows the mean mixed-layer depth estimated from the KPP model

Fig. 13 Vertically integrated dEHF (eastward positive toward the islands) over the mixed layer from ROMS-L2 along transect AA' (as shown in **Fig. 5f**). The black line indicates the mean position of the Kuroshio axis.

Table. 1 Computational configurations for the ROMS-L1 and ROMS-L2 models.

Models	L1	L2
Computational period	1/1/2005-9/14/2013	12/27/2010-9/14/2013
Grid cells	768× 768 (×32 layers)	832×608 (×32 layers)
Horizontal grid resolution	3.0 km	1.0 km
Baroclinic time step	240 sec	60 sec
Surface wind stress	QuikSCAT-ECMWF (daily, till 12/31/2007) JMA GPV-GSM (daily, 1/1/2008 and later)	JMA GPV-MSM (hourly)
Surface flux	COADS (monthly climatology)	
SST and SSS to restore	JCOPE2 (20-day averaged)	
Major river discharges (Yangtze River)	monthly climatology	—
Boundary/Initial condition	JCOPE2 (daily)	ROMS-L1 (daily)
TS nudging	JCOPE2 (10-day averaged)	—
Topography	SIO SRTM30_Plus	

Table. 2 Seasonally averaged volume flux in Sverdrup across the PN Line from the in situ observations, JCOPE2, ROMS-L1, and ROMS-L2 models.

	Spring	Summer	Fall	Winter
observation	26.4	26.9	25.1	26.0
JCOPE2	30.0	32.9	31.4	31.0
ROMS-L1	27.8	29.5	27.4	29.2
ROMS-L2	27.9	29.2	27.3	28.0

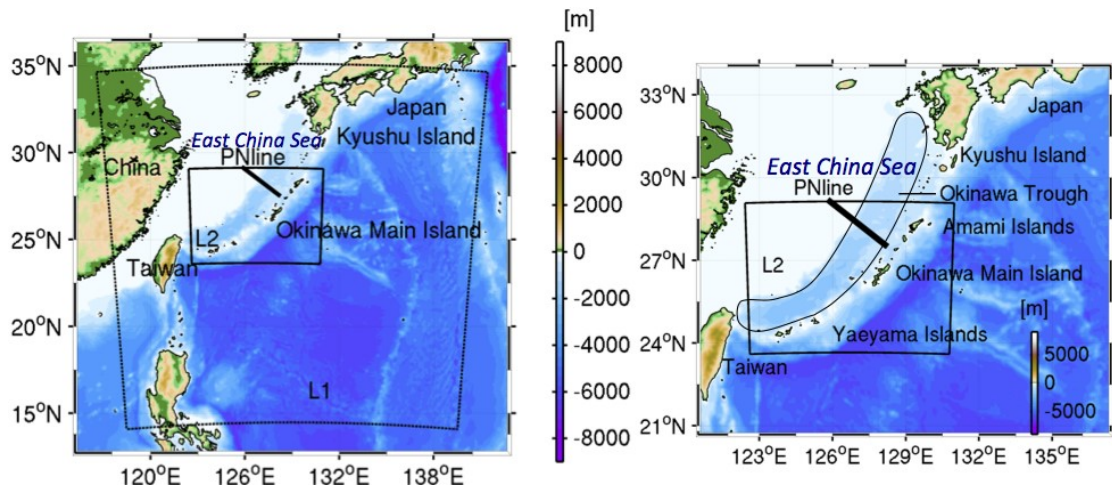


Fig. 1 Double-nested ROMS model domains and bathymetry (color: m). Left: the ROMS-L1 and L2 domains embedded in the JCOPE2 domain. Right: a zoomed-in region of the ROMS-L2 domain. Black thick line indicates the JMA PN Line transect.

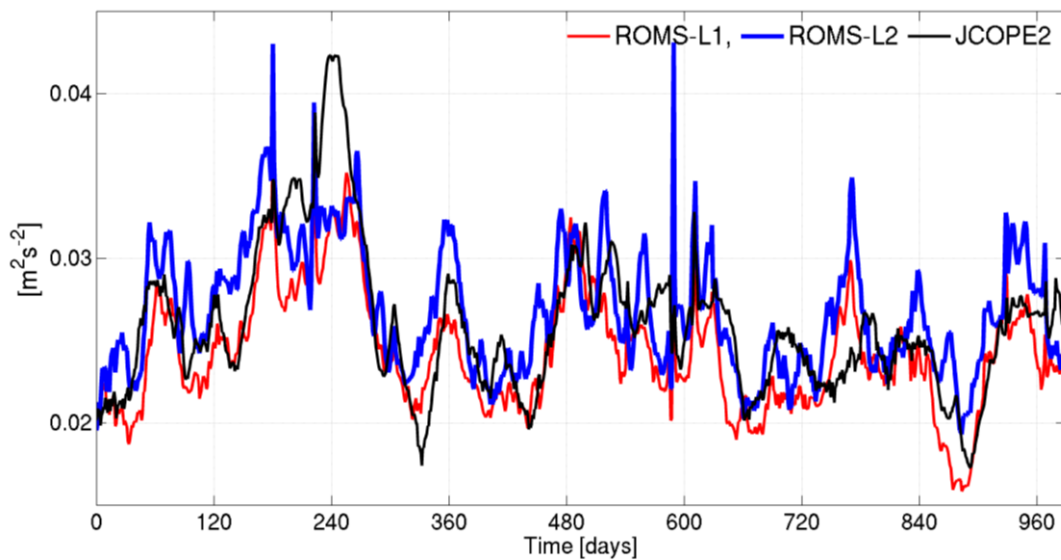


Fig. 2 Time series of the volume-averaged surface ($z > -400$ m) kinetic energy from the ROMS-L1 (red), ROMS-L2 (blue), and JCOPE2 (black) models. The abscissa indicates the elapsed time in days since December 27, 2010, UTC.

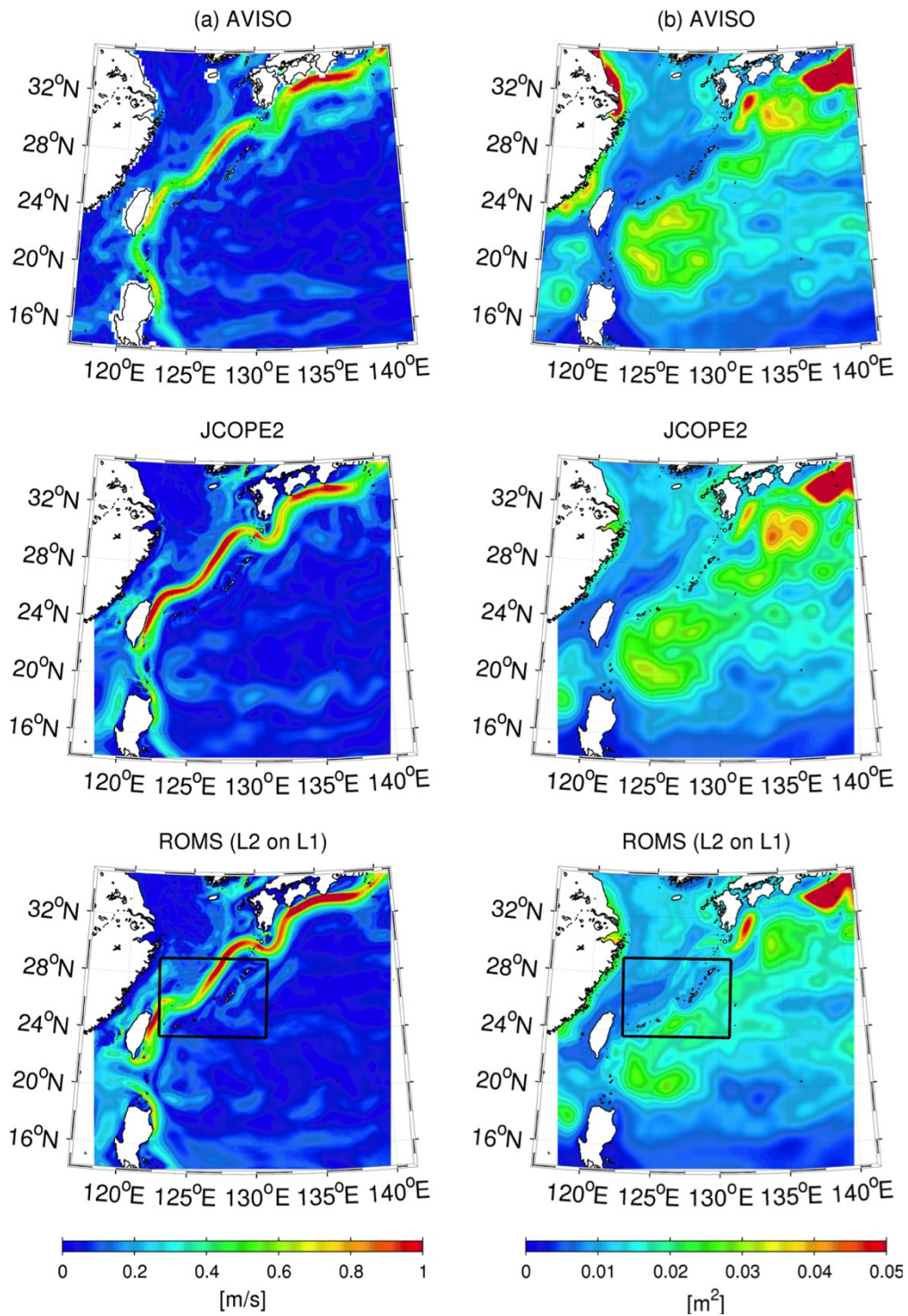


Fig. 3 Plan view plots of: (a) time-averaged surface velocity magnitude and (b) SSH variance. Top: AVISO data, middle: JCOPE2, and bottom: ROMS-L2 on L1.

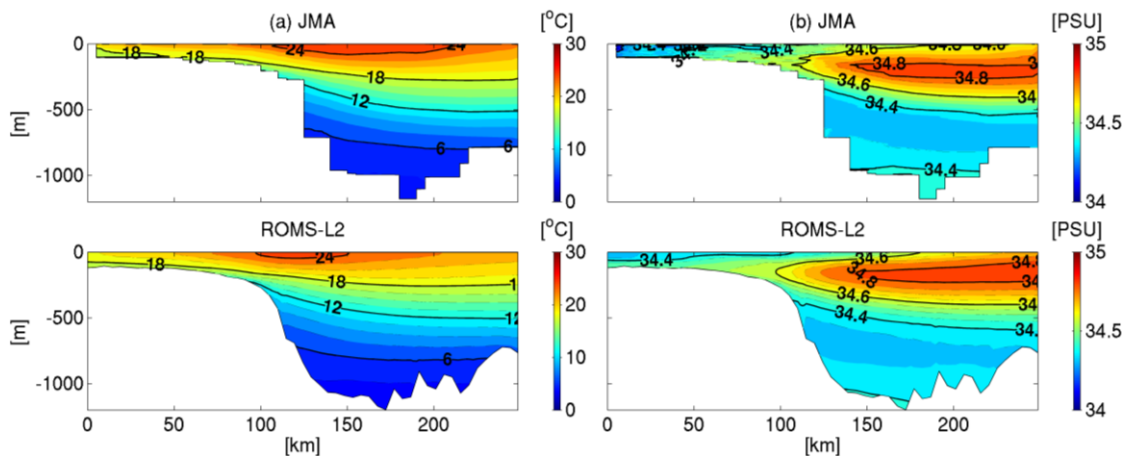


Fig. 4 Seasonally averaged temperature (left) and salinity (right) for spring from JMA observations (upper panels) and ROMS-L2 (lower panels) in the vertical section along the PN Line.

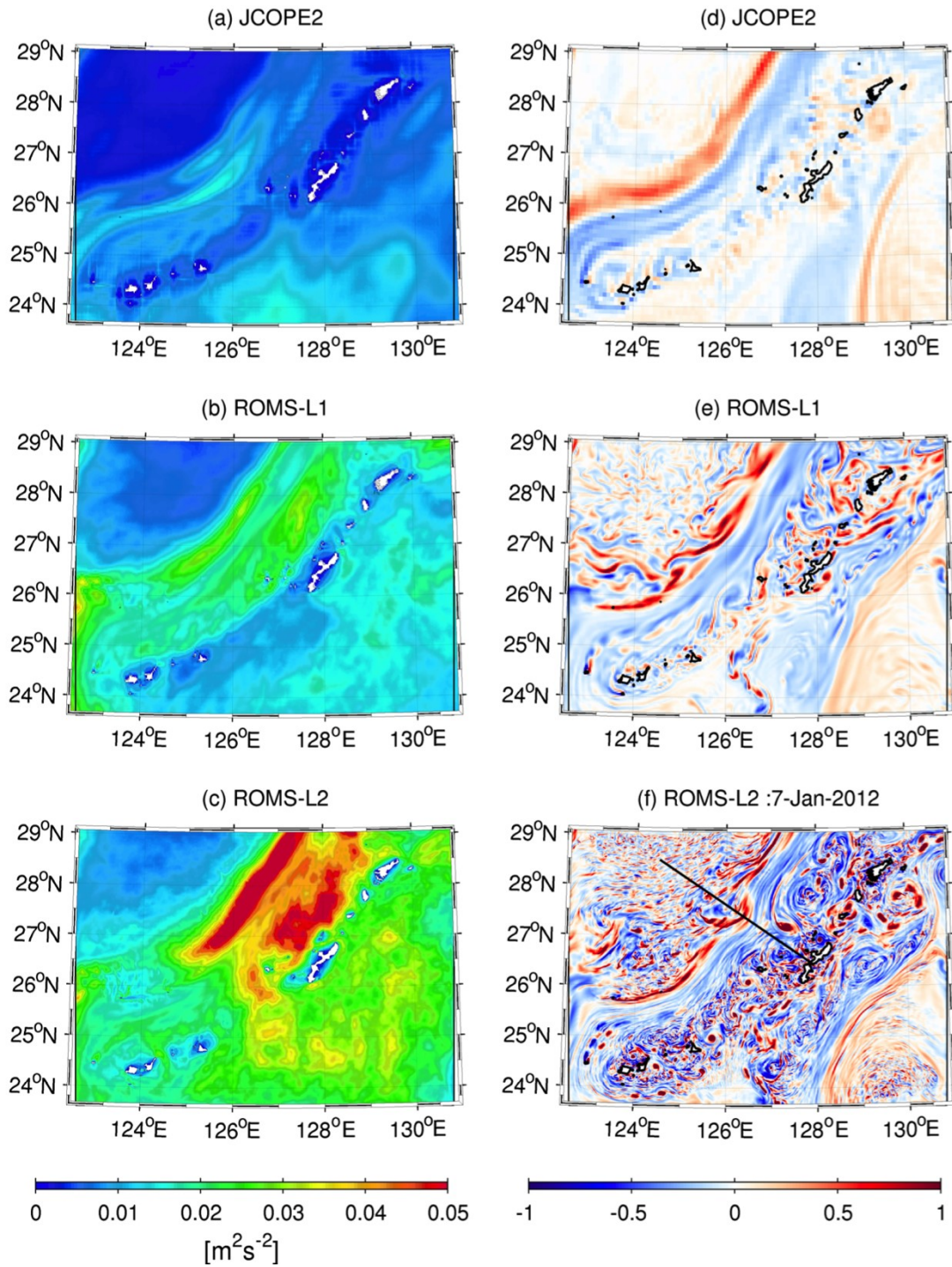


Fig. 5 Left panels—surface eddy kinetic energy (EKE), K_e , from: (a) JCOPE2, (b) ROMS-L1, and (c) ROMS-L2. Right panels—instantaneous spatial distributions of surface vorticity normalized by planetary vorticity, ζ/f (dimensionless) on January 7, 2012 from: (d) JCOPE2, (e) ROMS-L1, and (f) ROMS-L2. The black line in (f) indicates transect AA' for the cross-sectional plots.

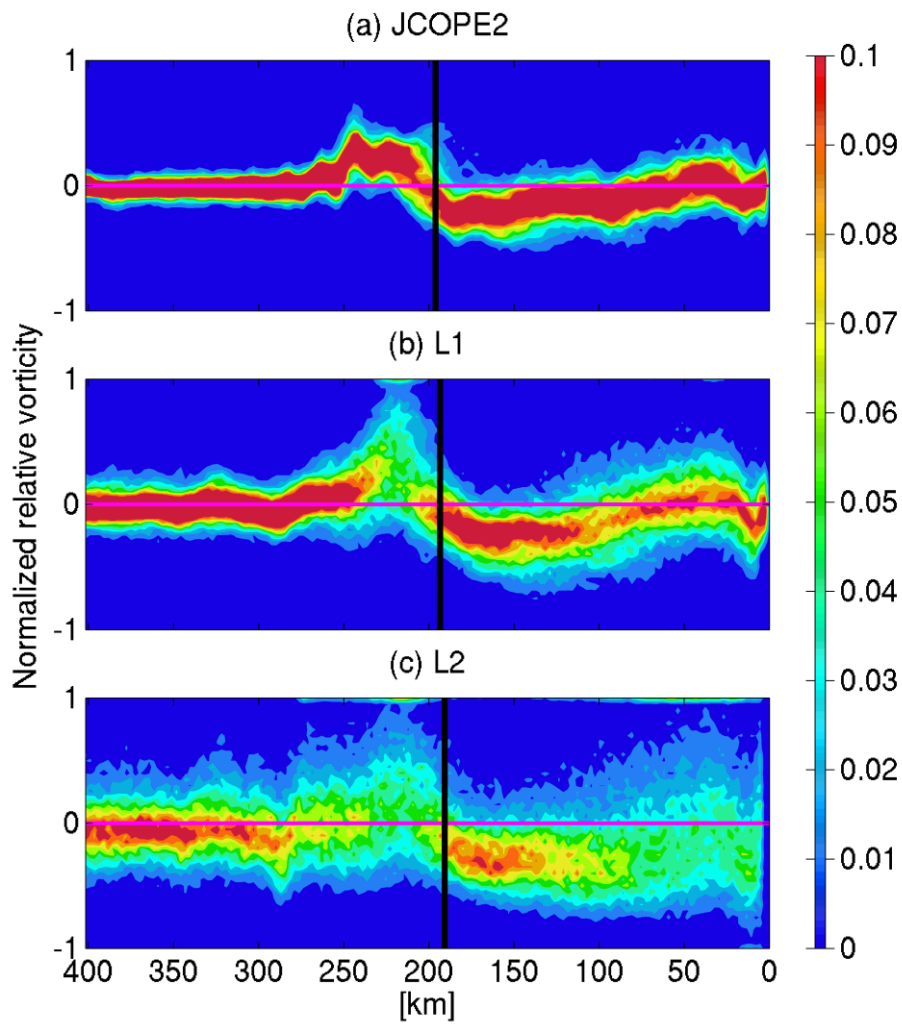


Fig. 6 Probability density functions of the normalized relative vorticity at 2 m depth along transect AA' (see Fig. 5f) from: (a) JCOPE2, (b) ROMS-L1, and (c) ROMS-L2 models, as a function of distance from Okinawa Island (km). The black lines are the mean Kuroshio axes.

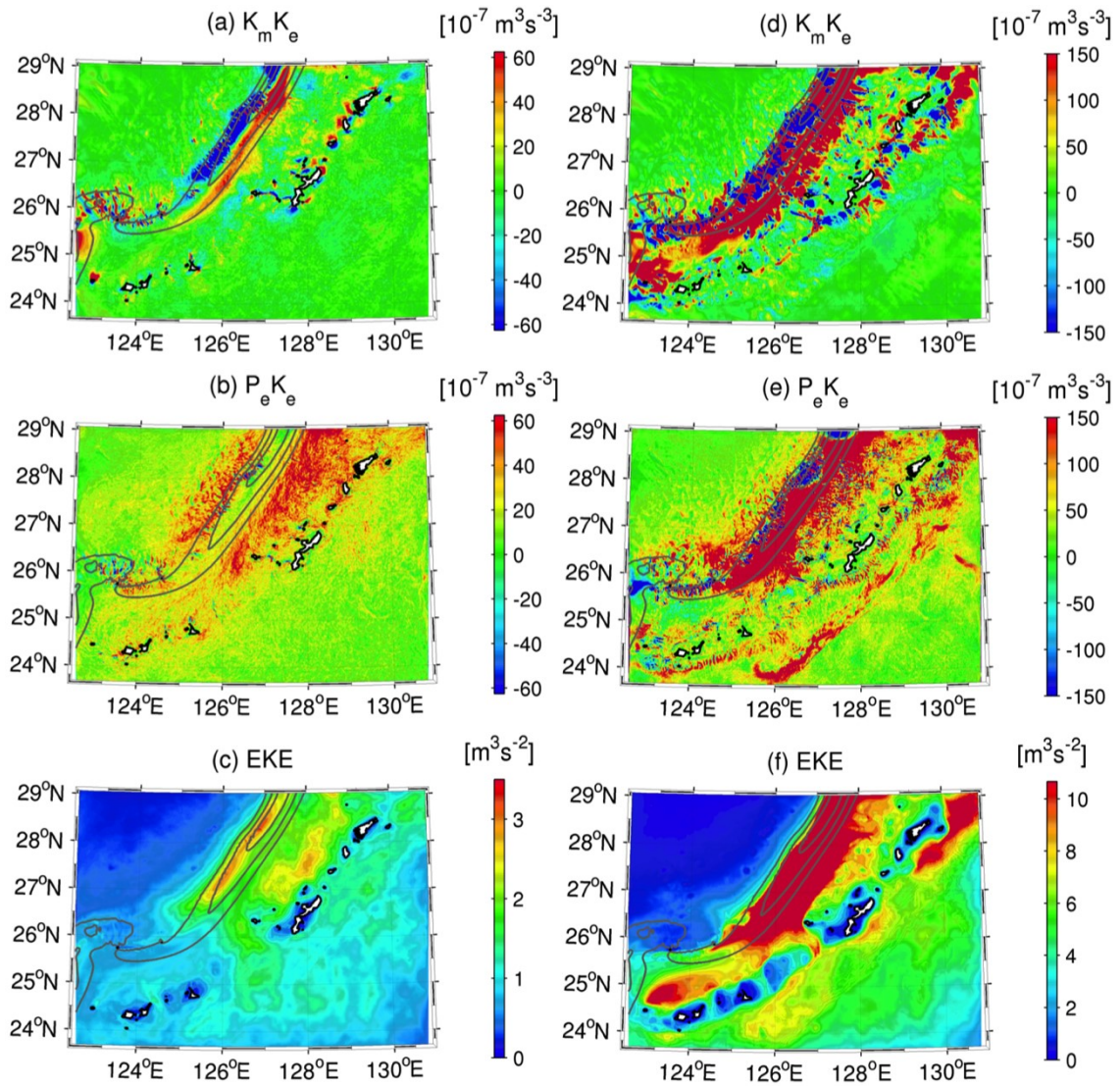


Fig. 7 Left panels: (a) barotropic conversion rate, $K_m K_e$, (b) baroclinic conversion rate, $P_e K_e$, and (c) EKE, K_e , integrated vertically over the mixed layer from the ROMS-L2 model results. Right panels: same as the left panels, but integrated vertically from the surface down to 1200 m depth. The gray contours represent surface velocity magnitude >0.5 m/s with intervals of 0.25 m/s.

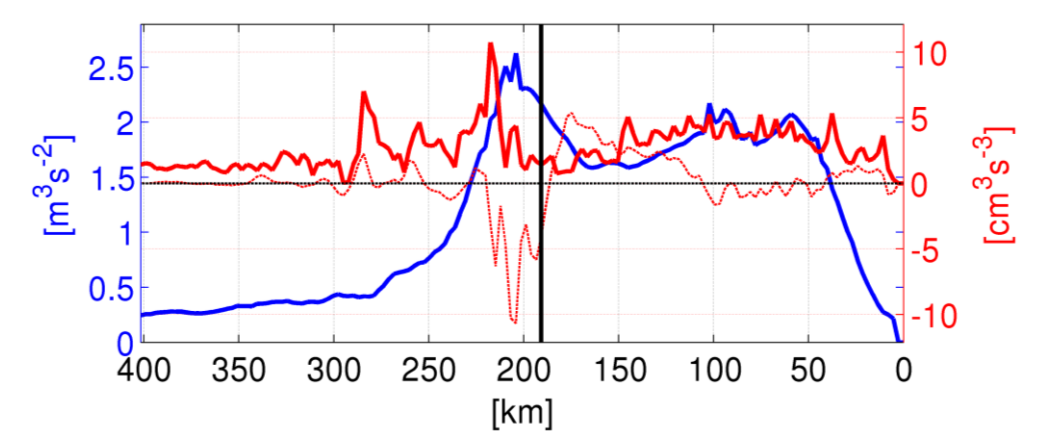


Fig. 8 Vertically integrated $K_m K_e$ (red thin line), $P_e K_e$ (red thick line) and K_e (blue line) over the mixed layer from ROMS-L2 along the transect shown by the black line in **Fig. 5f**. The black line indicates the mean position of the Kuroshio axis.

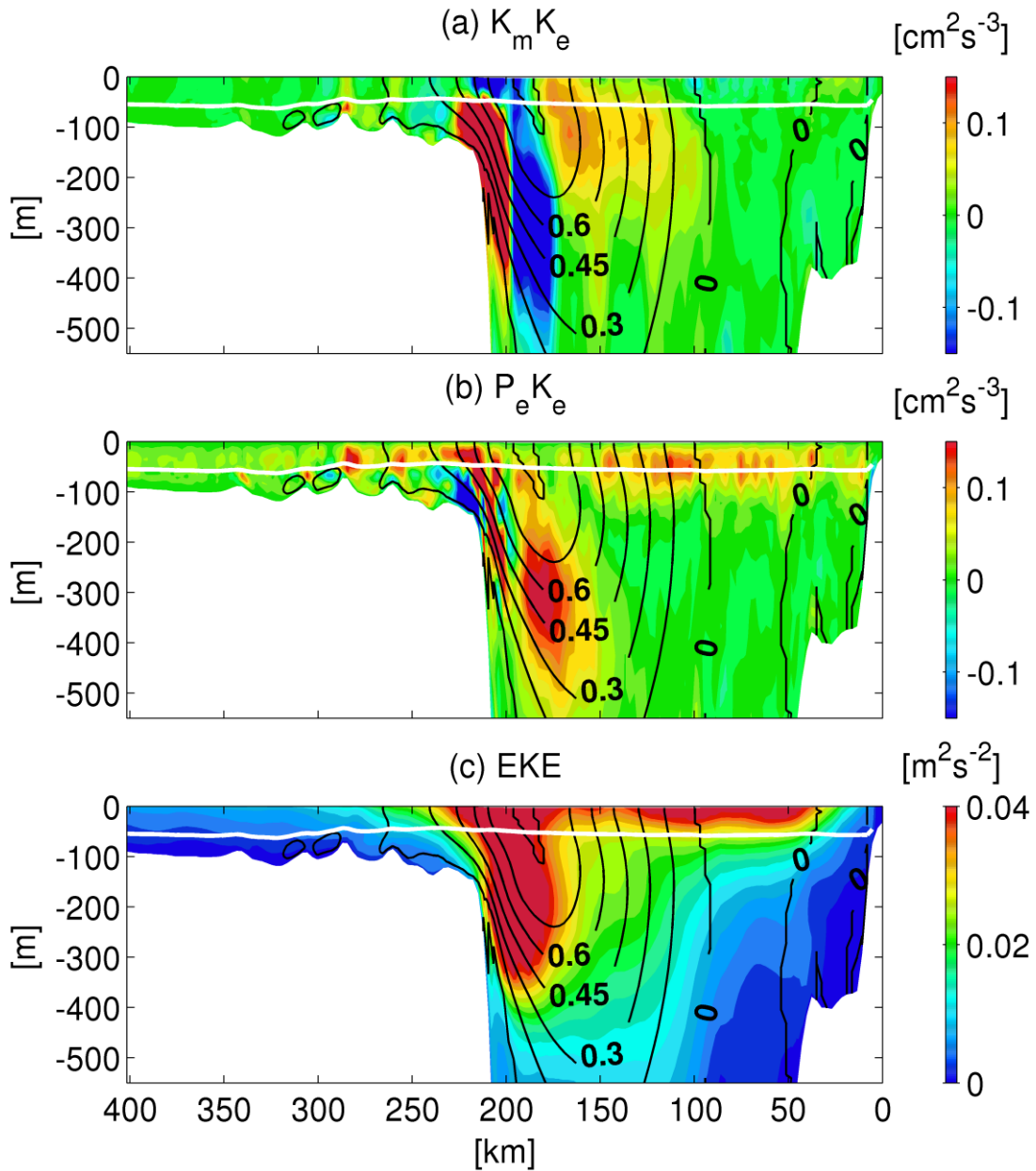


Fig. 9 Cross-sectional plots of: (a) barotropic conversion rate, $K_m K_e$, (b) baroclinic conversion rate, $P_e K_e$, and (c) EKE, K_e , from the ROMS-L2 model. The corresponding transect is shown by the black line in **Fig. 5f**. The white lines are the mean mixed-layer depth estimated from the KPP model in ROMS. The black contours represent the mean streamwise velocity normal to the transect.

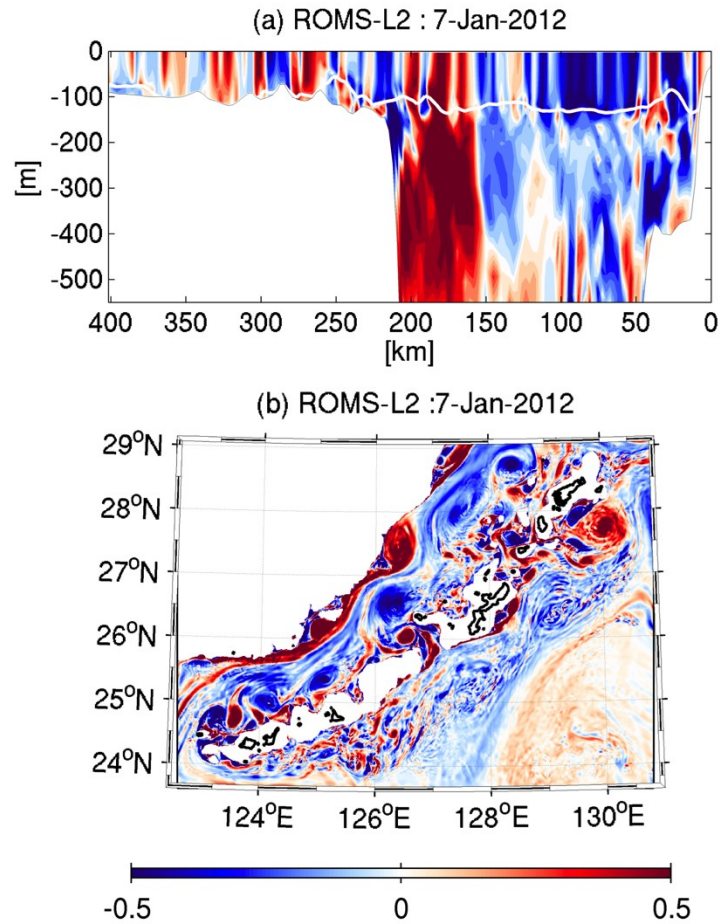


Fig. 10 (a) Cross-sectional plot of normalized relative vorticity ζ/f on January 7, 2012, along transect AA' (shown by the black line in **Fig. 5f**). The white line is the mixed-layer depth estimated from the KPP model. (b) Normalized relative vorticity ζ/f in the horizontal plane at $z = -400$ m on January 7, 2012.

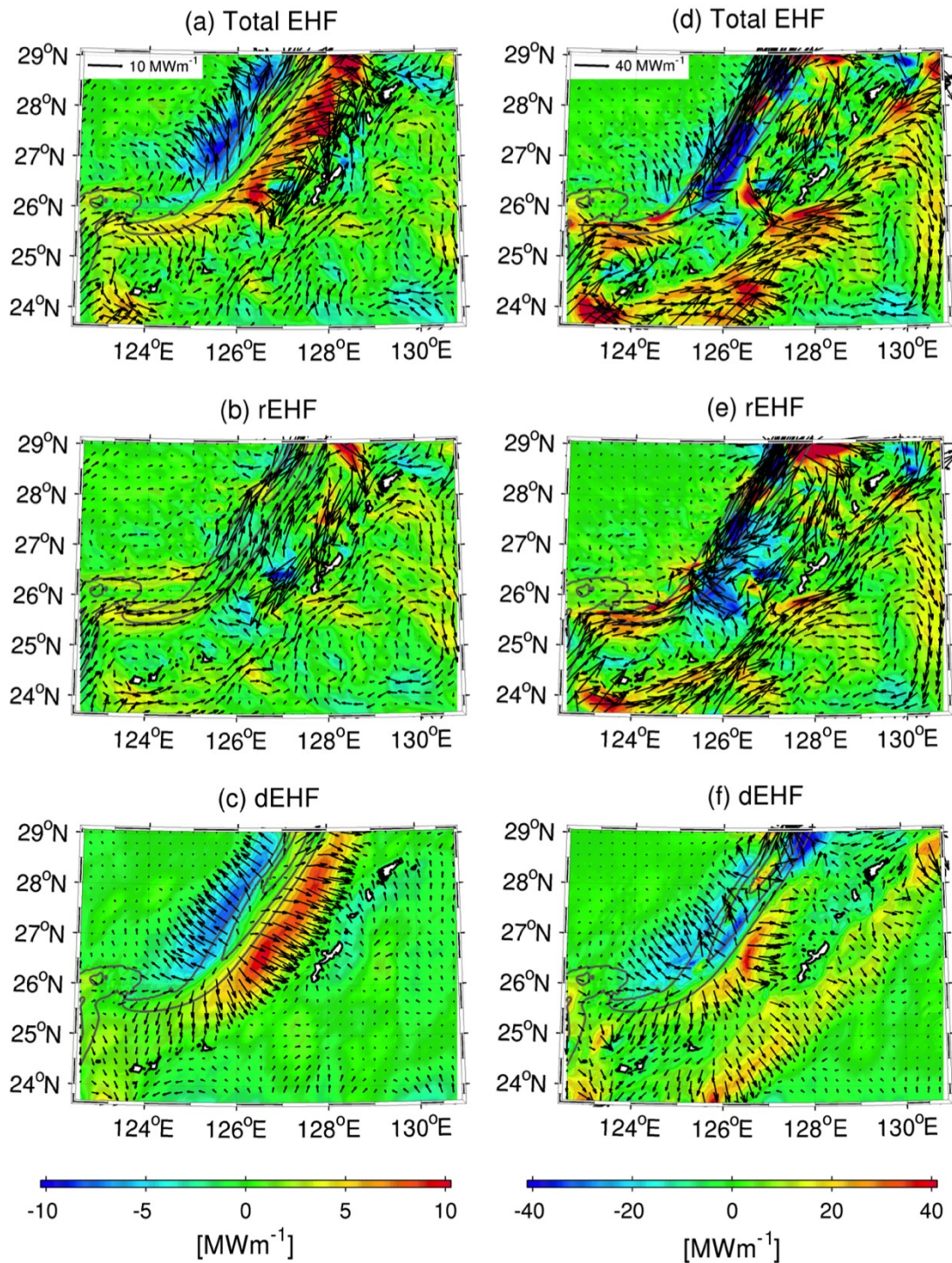


Fig. 11 Eddy heat flux (EHF) vectors vertically integrated (left) over the mixed layer and (right) from the surface to depth of 1200 m, superposed on the across-Kuroshio component of the labeled EHF (in color). (upper) total EHF, (middle) rotational component, rEHF, and (lower) divergent component, dEHF. The gray contours are surface velocity magnitude >0.5 m/s with intervals of 0.25 m/s.

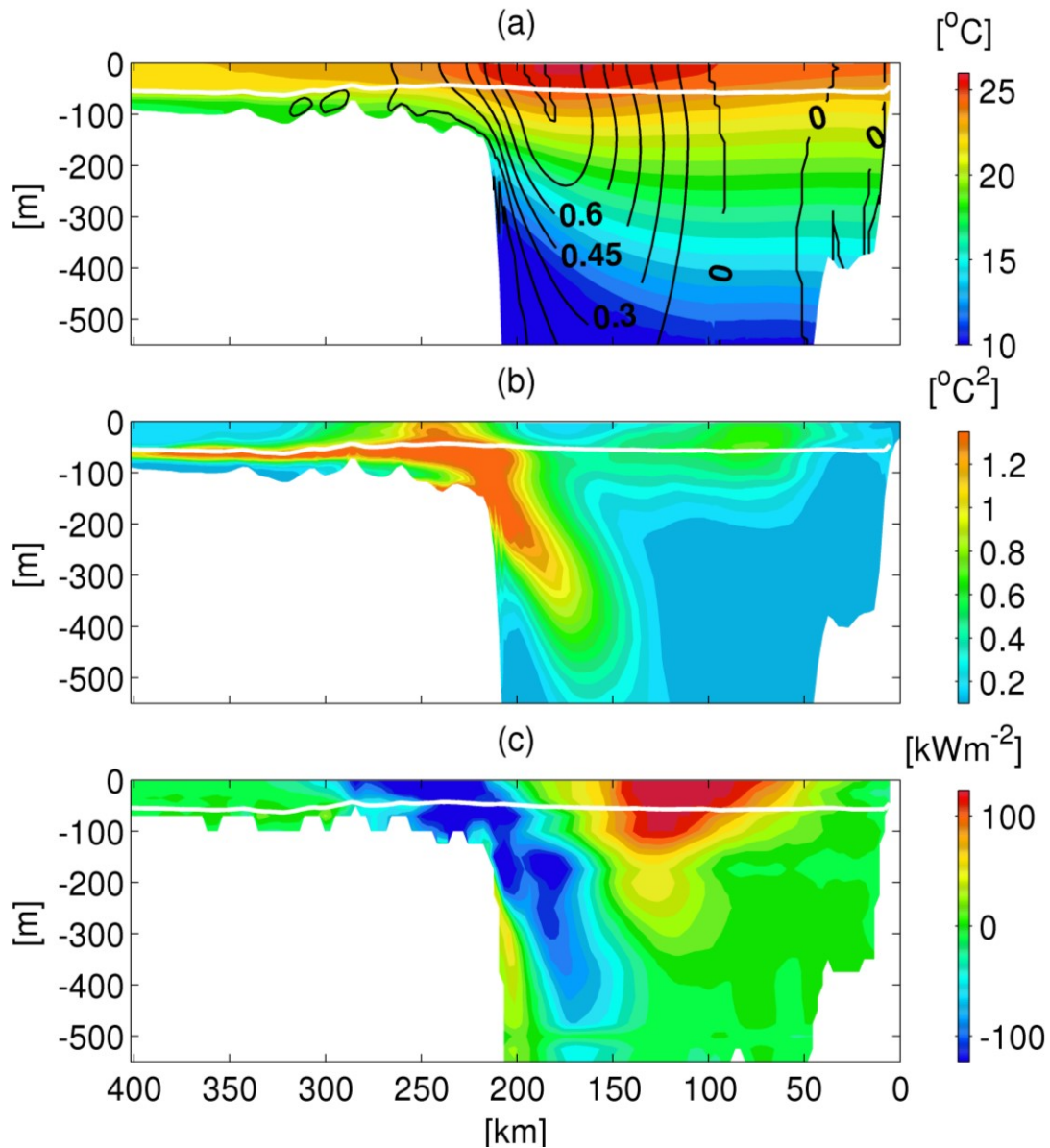


Fig. 12. Cross-sectional plots of: (a) mean streamwise velocity normal to the transect (contours) and mean temperature (color), (b) temperature variance, and (c) across-Kuroshio component of the divergent eddy heat flux, dEHF (eastward positive toward the islands) from the ROMS-L2 results, along the transect shown by the black line in **Fig. 5f**. White line shows the mean mixed-layer depth estimated from the KPP model

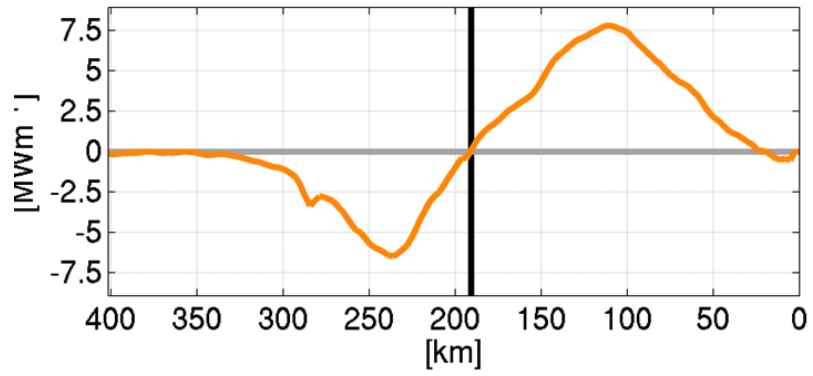


Fig. 13 Vertically integrated dEHF (eastward positive toward the islands) over the mixed layer from ROMS-L2 along transect AA' (as shown in **Fig. 5f**). The black line indicates the mean position of the Kuroshio axis.

Reserch Highlights

Oceanic simulation is conducted for the area around the Ryukyu Islands in ECS.
Topographic shear and baroclinic instability enhance submesoscale eddies in ECS.
Submesoscale eddies promote lateral material transport from Kuroshio.